# Mechanical Resistance in Unstructured Proteins

Sigurður Ægir Jónsson,[†] Simon Mitternacht,[‡] and Anders Irbäck[†*]
[†]Computational Biology & Biological Physics, Department of Astronomy and Theoretical Physics, Lund University, Lund, Sweden; and
[‡]University Library, University of Bergen, Bergen, Norway

ABSTRACT   Single-molecule pulling experiments on unstructured proteins linked to neurodegenerative diseases have measured rupture forces comparable to those for stable folded proteins. To investigate the structural mechanisms of this unexpected force resistance, we perform pulling simulations of the amyloid $\beta$-peptide (A$\beta$) and $\alpha$-synuclein ($\alpha$S), starting from simulated conformational ensembles for the free monomers. For both proteins, the simulations yield a set of rupture events that agree well with the experimental data. By analyzing the conformations occurring shortly before rupture in each event, we find that the mechanically resistant structures share a common architecture, with similarities to the folds adopted by A$\beta$ and $\alpha$S in amyloid fibrils. The disease-linked Arctic mutation of A$\beta$ is found to increase the occurrence of highly force-resistant structures. Our study suggests that the high rupture forces observed in A$\beta$ and $\alpha$S pulling experiments are caused by structures that might have a key role in amyloid formation.

## INTRODUCTION

The amyloid-forming proteins linked to neurodegenerative disorders often belong to the class of intrinsically disordered proteins (1–4). Recent single-molecule AFM experiments show that, despite their lack of a well-defined folded structure, such proteins sometimes exhibit high mechanical resistance when pulled by an applied force (5–7). Rupture forces of similar magnitude are, in fact, only rarely observed for folded proteins (8,9). In this article, we attempt to convince the reader that subensembles of folded conformations with a specific architecture can explain this unexpected force-resistance.

The pathway from a more or less disordered monomer to an ordered amyloid fibril, with its characteristic cross-$\beta$ structure, involves a host of intermediate assemblies. The exact character of these species, and their possible roles in pathogenesis, is not completely understood (10–12). It is, however, clear that at some point the assemblies become rich in $\beta$-sheets. Structural motifs, and in particular $\beta$-sheets, are key to the mechanical stability of proteins. In general, the response to a stretching force is largely dictated by native topology (13,14) and pulling geometry (15,16), and high stability can be traced to a specific structural unit, a mechanical clamp (8). Typically, these units are $\beta$-sheets, arranged such that the strands cannot be separated without breaking a number of hydrogen bonds all at once. The AFM-detected force-resistant states of disease-related proteins (5–7) therefore appear likely to contain $\beta$-sheets, and could play a vital role in the aggregation process. Knowledge of the structural specifics of the force-resistant states could thus provide valuable and general insight into the aggregation mechanisms in amyloid diseases.

In this study, we use atomic-level Monte Carlo (MC) simulations to search for and characterize possible mechanical clamps in Alzheimer's amyloid $\beta$-peptide (A$\beta$) and the Parkinson's disease-linked $\alpha$-synuclein protein ($\alpha$S). Both proteins are unstructured and amyloid-forming, and displayed mechanical resistance in AFM experiments (5–7). Computational modeling offers unique opportunities to interpret this force response, but requires the use of large sets of trajectories, due to the structural diversity of the proteins. Our calculations are carried out starting from large and diverse sets of initial conformations, randomly drawn from previously simulated ensembles (17,18). In the simulations, high-force rupture events occur for both proteins. We find that these events are caused by one specific type of mechanical clamp, which shows similarities to the folds adopted by A$\beta$ (19,20) and $\alpha$S (21) in fibrils. Such structures could play an important role in the addition of monomers to growing A$\beta$ and $\alpha$S fibrils, an association that requires large parts of the monomers to adopt a specific fold. In addition to the wild-type (WT) sequences, we study the disease-related Arctic E22G mutant (22) of A$\beta$, and find it to increase the occurrence of strong mechanical clamps.

## METHODS

### Model

Our simulations are based on an all-atom implicit solvent model with torsional degrees of freedom (23). The energy function consists of four main terms:

$$E = E_{ev} + E_{loc} + E_{hb} + E_{sc}.$$

The $E_{ev}$ term represents excluded volume effects, whereas $E_{loc}$ handles local interactions among neighboring atoms. Hydrogen bonds between backbone NH and CO groups, and between charged side-chain groups and the backbone, are handled by $E_{hb}$. The last term, $E_{sc}$, represents interactions between side chains, both hydrophobic attraction and attraction/repulsion between charged side chains. The mathematical form and

---

parameters of the model are given elsewhere (23). The computational convenience of the model allows us to generate large sets of trajectories, which is important because of the conformational polymorphism of the proteins studied.

One of the big challenges in creating protein models is to obtain a realistic temperature dependence. The temperature scale of our model was determined to give correct folding temperatures for a diverse set of small peptides (23). Our simulations have, however, shown that the temperature scale needs recalibration for the larger A$\beta$ and $\alpha$S proteins (17,18). Below we will give the nominal temperatures used in the simulations and indicate what physical temperatures these correspond to, based on comparisons with experimental data.

## Pulling

We model the action of the pulling force by adding a harmonic potential in the end-to-end distance of the protein, $L(x)$ (between the first and last backbone atoms), where $x$ denotes a protein conformation. The equilibrium length is initially set to the end-to-end distance of the starting conformation, $L_0 = L(x_0)$, and then increases with a constant velocity $v$. The full energy function is given by

$$E_{\text{tot}}(x, t) = E(x) + \frac{k}{2}[L_0 + vt - L(x)]^2, \qquad (1)$$

where $E(x)$ is the energy in the absence of external force, $t$ is MC time, and $k$ is a spring constant. In our calculations, we set $k = 37$ pN/nm and $v = 0.05$ fm/MC step. The AFM study of A$\beta$ and $\alpha$S by Hervás et al. (7) was performed using an estimated cantilever stiffness of 30–70 pN/nm and a pulling speed of 0.4 nm/ms. Our $v$ cannot be directly translated to an experimental pulling speed, but was empirically chosen based on previous simulations of fibronectin domains (24). Here, we found simulation results obtained using $v = 0.1$ fm/MC step to be compatible with AFM measurements at a pulling velocity of 0.6 nm/ms. Therefore, in our calculations, we expect rupture forces comparable to those measured by Hervás et al. (7), especially because the velocity dependence is only logarithmic (25). Generating A$\beta$ and $\alpha$S unfolding trajectories at experimental pulling velocities by conventional molecular-dynamics methods is a challenge, as the required time span of each trajectory is ~0.1 s.

## MC details

We simulate the above model using MC dynamics. MC is a crude approximation to the real dynamics over short timescales, but we expect MC-based unfolding simulations to capture the major free-energy minima and barriers encountered by a protein when stretched, provided that only small trial moves are used (26,27). Our calculations are based on two small-step MC updates: rotations of single side-chain angles and coordinated Biased Gaussian Steps for backbone angles (28). Biased Gaussian Steps updates up to eight consecutive backbone torsion angles in a manner that keeps the ends of the updated segment approximately fixed. The equilibrium length of the harmonic spring pulling the protein is increased by a small constant amount in each MC step.

## A$\beta$ ensembles

We study the highly amyloidogenic 42-residue form of A$\beta$. In previous work, we investigated monomer properties and dimer formation for four variants of this peptide: WT, E22G, F20E, and E22G/I31E (17,29). The model temperature (nominally 37°C) was chosen for best match with experimental chemical shifts (30) and $J$-couplings (31) measured at 0–5°C. This study is conducted at the same temperature, and focuses on the WT and E22G variants. To ensure proper sampling, new extended simulations of the free monomers were performed, which indeed agree very well with pre-

vious data. Starting from conformations randomly drawn from these equilibrium ensembles, a set of 512 independent pulling trajectories was generated for each of WT A$\beta$ and E22G A$\beta$.

## $\alpha$S ensemble

In our previous study of the free 140-residue $\alpha$S monomer, we observed two distinct phases: a disordered high-energy phase, D, and a $\beta$-structure-rich low-energy phase, B (18). The transition frequency between these phases was insufficient for a determination of their relative fraction as a function of temperature. Our analysis therefore focused on single-phase properties, evaluated using a fixed model temperature (nominally 56°C) at which both phases coexisted. The generated D-phase ensemble was found to be in good agreement with NMR data at 15°C (32). A consistent description of NMR data at −15°C and −10°C (33,34) in terms of the B and D phases was, by contrast, found to require a significant B-phase fraction, ~50–70%. Our pulling simulations are carried out using the same model temperature (56°C), with initial conformations randomly drawn from the two single-phase equilibrium ensembles (total number 1024). As in the previous study, the two phases are analyzed separately.

## Analysis

In the pulling simulations, we monitor the external force, $F$, and the end-to-end distance, $L$. Some examples of force-distance trajectories can be found in Fig. 1. In our analysis of the generated trajectories, the data are noise-filtered using a sliding window of size $T_w = 6 \times 10^6$ MC steps. We identify rupture events as sudden drops in force with MC time. To discriminate true rupture events from noise, we require the force to drop by >20 pN within a time interval of $T_w$, from a peak value >20 pN (the force can drop to negative values). For each rupture event, we register the maximum force, $F_r$, and the end-to-end distance, $L_r$, at which the peak occurs.

Secondary structure is classified using the program STRIDE (35). The $\beta$-structure content is calculated as the fraction of residues that are in the class extended. Solvent accessibility calculations are performed using the software program NACCESS (36).

To locate $\beta$-hairpin turns, a contact-based measure of turn propensity, $\tau_i$, is calculated. Two residues are said to be in contact if two or more heavy-atom pairs are within 4.5 Å of each other. The measure $\tau_i$ is defined as the sum of all contact probabilities $p_{jk}$ in a strip perpendicular to the main diagonal of the contact map, $2(i − 1) < j + k < 2(i + 1)$.

Figures of three-dimensional structures are drawn using the software PYMOL (37).

## RESULTS

### WT A$\beta$

The A$\beta$ molecule is small and natively unfolded, and may seem unlikely to exhibit any mechanical resistance. However, in their AFM study, Hervás et al. (7) found that many unfolding traces contained at least one force peak >20 pN. The maximum recorded rupture force exceeded 300 pN.

We examine the structural mechanisms causing this force resistance using MC simulations. As described in Methods, starting from a simulated ensemble of conformations, we study the response of the protein when pulled at constant velocity. In some of the simulated trajectories, when stretched, the A$\beta$ molecule gets trapped in a force-resistant state, the breaking of which gives rise to a force maximum (Fig. 1). Rupture events, signaled by force peaks >20 pN,
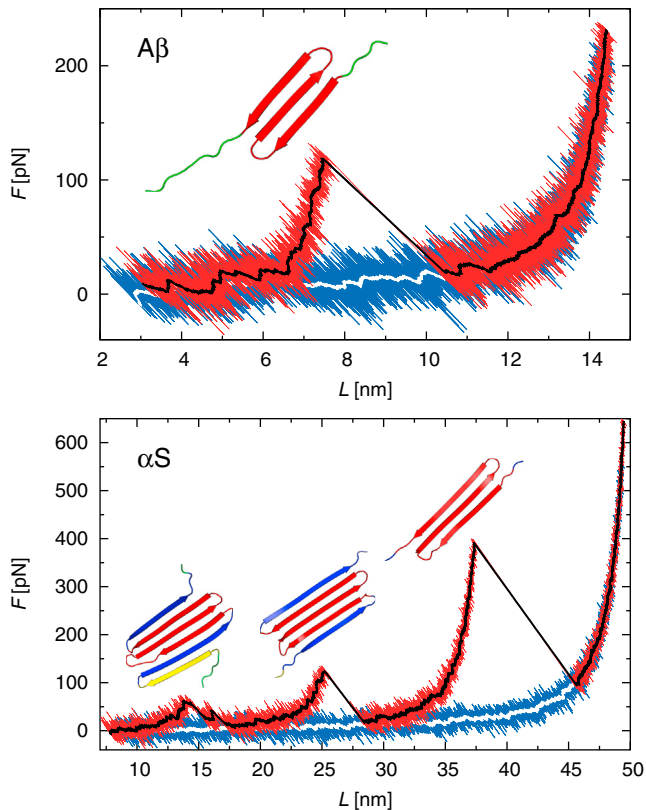
FIGURE 1 Examples of simulated unfolding trajectories. (*Upper panel*) Force, $F$, versus end-to-end distance, $L$, in two runs for WT A$\beta$. In one trajectory, no force-resistant state is encountered as the molecule is stretched. In the other, a rupture event occurs at $L_r = 7.5$ nm and $F_r = 119$ pN. The three-dimensional structure is a snapshot just before the rupture event. (*Thick curves*) Representation of noise-filtering used when analyzing the data (see Methods). (*Lower panel*) Similar plot showing two $\alpha$S trajectories with zero and three rupture events, respectively. The three-dimensional structures are snapshots before the rupture events. The first structure shows residues 1–101, whereas the final three-stranded $\beta$-sheet is formed by the 33–85 segment.

occur in 148 of our 512 unfolding trajectories (see Methods for a description of our peak detection protocol). Most of these 148 runs contain one rupture event, but there are also trajectories with two such events (Table 1). For each rupture event, we record the maximum force, $F_r$, and the end-to-end distance, $L_r$, at which the peak occurs. The distributions of $F_r$ and $L_r$ are broad (Fig. 2), showing that

**TABLE 1   Rupture event statistics**

| Protein | $N_{\text{traj}}$ | $N_{\text{mech}}$ | $N_{\text{ev}}$ |
|---|---|---|---|
| A$\beta$ WT | 512 | 148 (135, 13, 0, 0, 0) | 161 |
| A$\beta$ E22G | 512 | 172 (144, 27, 1, 0, 0) | 201 |
| $\alpha$S, D phase | 449 | 2 (1, 1, 0, 0, 0) | 3 |
| $\alpha$S, B phase | 575 | 563 (37, 205, 274, 43, 4) | 1461 |

The total number of trajectories ($N_{\text{traj}}$), the number of trajectories with at least one rupture event ($N_{\text{mech}}$), and the total number of observed rupture events ($N_{\text{ev}}$) for the four systems studied. The numbers of trajectories with 1, 2, 3, 4, and 5 rupture events are indicated within parentheses in the $N_{\text{mech}}$ column.
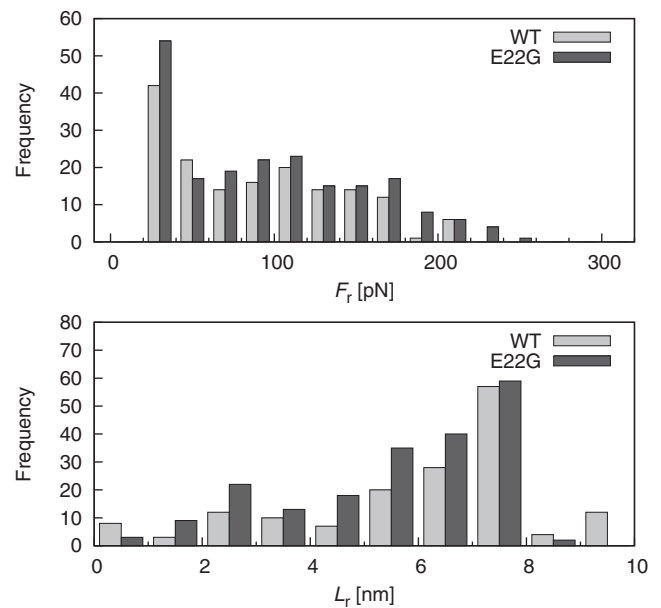


FIGURE 2   Histograms of rupture force (*upper panel*), $F_r$, and rupture distance (*lower panel*), $L_r$, for WT and E22G A$\beta$, based on 161 and 201 rupture events, respectively.

the observed rupture events are caused by a range of structures with varying mechanical strength. Our simulations differ in several details from experiments, where, for instance, the molecule of interest is embedded in a multimodular construct. Despite these uncertainties, our results are in good overall agreement with those reported by Hervás et al. (7). The conformational polymorphism that we observe resembles that found in the experiments, and our measured rupture forces are comparable to the experimental ones.

Having seen this agreement, we next examine the structures causing the simulated rupture events. What conformational features give rise to rupture forces as high as 210 pN (Fig. 2)?

The starting conformations for our pulling simulations are drawn from a diverse equilibrium ensemble, generated as described in Methods. Fig. 3 shows the free energy of this ensemble, calculated as a function of accessible surface area and $\beta$-structure content. Two major free-energy minima can be identified, both shallow and broad. One minimum corresponds to single extended $\beta$-sheets and the other to more compact, often double-layered structures, with lower accessible surface area ($<36$ nm$^2$) and lower $\beta$-structure content ($<0.5$). The plot symbols in Fig. 3 represent the conformations from which our pulling simulations are started, and indicate the magnitude of the maximum rupture force along the respective trajectories. A majority of the trajectories containing rupture events start out from the free-energy minimum corresponding to single extended $\beta$-sheets. Conformations from the other minimum have shorter $\beta$-strands and are typically unable to withstand high forces.
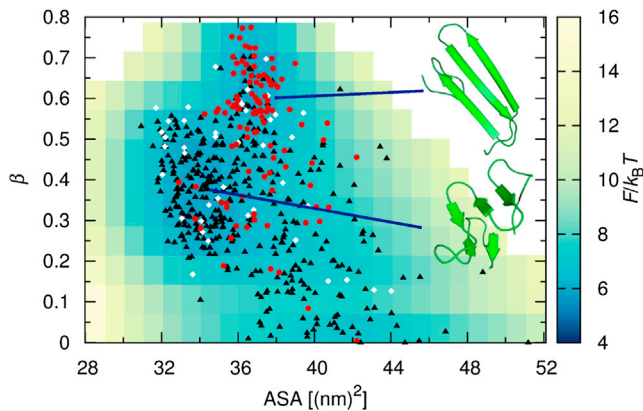
FIGURE 3 Equilibrium free energy, $F(ASA, \beta)$, calculated as a function of accessible surface area, $ASA$, and $\beta$-structure content, $\beta$, for WT A$\beta$. (*Plot symbols*) Starting structures for the pulling simulations, using averages of $ASA$ and $\beta$ over a short time interval ($6 \times 10^6$ MC steps). The plot symbol indicates whether the maximum rupture force along the corresponding pulling trajectory is <20 pN (*triangle*), 20–150 pN (*diamond*), or >150 pN (*circle*). The free energy has two shallow minima. The three-dimensional structures represent these minima.

To pinpoint the structural elements providing mechanical resistance, we examine the conformations sampled just before the rupture events. An analysis of secondary-structure content before rupture shows that high rupture forces occur only if the $\beta$-structure content is high (Fig. 4). For a more detailed picture, we divide the rupture events into four classes based on $\beta$-sheet geometry, as indicated by the plot symbols in Fig. 4. The first two classes correspond to three-stranded $\beta$-sheets with specific turn locations (turns are identified using the measure $\tau_i$ defined in Methods). The turns are located in the 13–15 and 23–24 intervals for the first class, and in the 13–15 and 25–27 intervals for the second class. The third class represents all three-stranded $\beta$-sheets with other turn locations. These three classes all contain many high-$F_r$ events, and the average $F_r$ is > 100 pN in all three cases. The fourth and last class collects all the remaining rupture events. The corresponding structures are often double-layered, and sometimes contain smaller $\beta$-sheets. For this class, the average rupture force is ~40 pN. This analysis confirms that most of the main mechanical clamps are three-stranded $\beta$-sheets. Typically, they have a simple meander topology. Beta-sheets with an odd number of strands in a meander pattern are indeed obvious candidates for mechanical clamps. Unlike a $\beta$-hairpin, they cannot be unzipped one hydrogen bond at a time.

The three-stranded $\beta$-sheets causing rupture events share similar sequence locations, as one might expect for a small protein such as A$\beta$. To quantify this, we show in Fig. 5 a $\beta$-structure profile, obtained by averaging over structures just before rupture in all events involving three-stranded $\beta$-sheets. The profile shows that there indeed are statistically preferred turn and strand regions. In addition, it can be
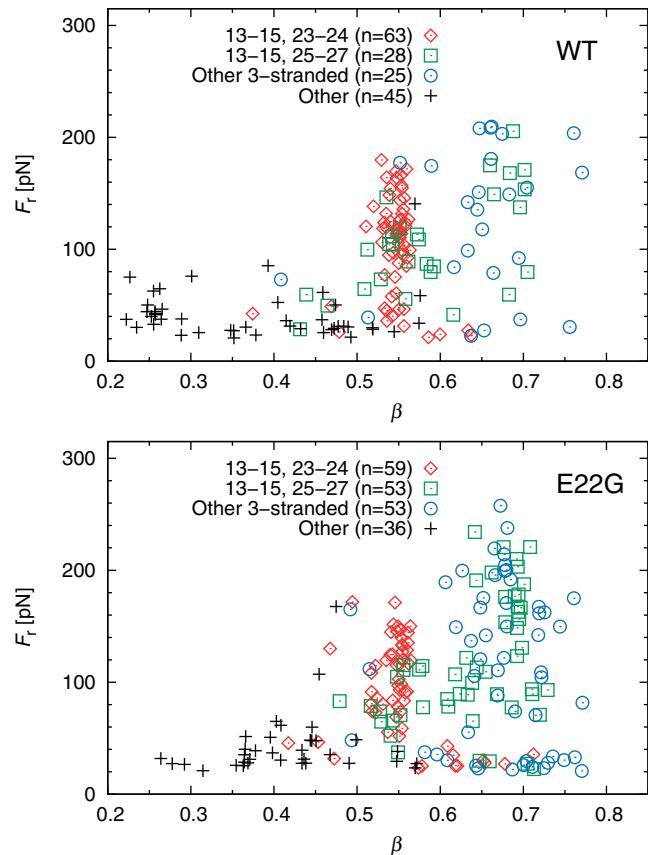


FIGURE 4 Scatter plots of rupture force, $F_r$, and $\beta$-structure content, $\beta$, for WT (*upper panel*) and E22G (*lower panel*) A$\beta$. The quantity $\beta$ is an average over a short time interval ($6 \times 10^6$ MC steps) just before the rupture event. (*Plot symbols*) Four conformational classes. The first two correspond to three-stranded $\beta$-sheets with specific turn locations. The third class represents extended three-stranded $\beta$-sheets with other turn locations. The fourth category consists of structures with, at most, two extended $\beta$-strands, some of which are double-layered.

seen that the second and third strand regions overlap with the two strand regions in A$\beta$ fibrils (19,20).

For a $\beta$-sheet to display mechanical resistance, its strands must be sufficiently long. In the case of A$\beta$, the required strand length can be achieved only if a large part of the whole molecule participates in the $\beta$-sheet. In fact, among the observed force peaks >100 pN for the two A$\beta$ variants, almost all are caused by structures with a $\beta$-structure content >0.5 (Fig. 4). By forming such structures, it becomes possible for A$\beta$, despite its small size, to withstand these high forces.

It is worth noting that these $\beta$-sheets still do not have maximal size. In WT A$\beta$ simulations at a lower temperature, we observed even larger three-stranded $\beta$-sheets ($\beta$-structure contents of ~0.8). In pulling simulations started from these conformations, we recorded rupture forces of up to 300 pN. However, these conformations are not significantly sampled at the temperature used in this study.
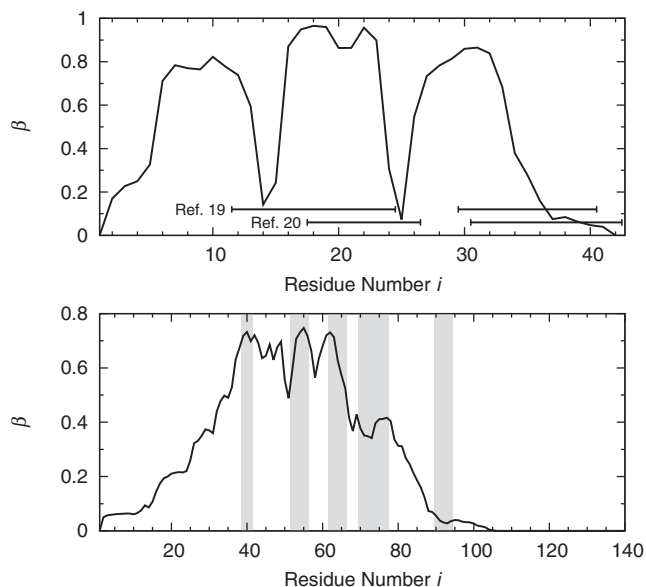
FIGURE 5   Average $\beta$-structure profiles for WT A$\beta$ (*upper panel*) and $\alpha$S (*lower panel*) rupture events involving three-stranded $\beta$-sheets. For each event, residue-specific $\beta$-structure propensities are computed over a short time interval (6 $\times$ 10$^6$ MC steps) just before rupture. A second average over events gives the final profile. (*Upper panel, horizontal bars*) Strand regions in A$\beta$ fibrils as obtained by Petkova et al. (19) and Lührs et al. (20). (*Lower panel, shaded vertical bars*) Strand regions in $\alpha$S fibrils (21).

## Arctic A$\beta$

Having identified candidate structures for mechanical resistance, it is still not clear what relevance these have for aggregation and disease. A natural next step is to study how the force response is altered by disease-related mutations, such as the (Arctic) E22G mutation. The experiments by Hervás et al. (7) found this mutation to lead to an increased occurrence of force-resistant states. The highest force peak was >400 pN, indicating the breaking of a "hyper-mechanostable" conformation.

We study E22G A$\beta$ using the same setup as for WT A$\beta$, and see many similarities between the two variants, as is expected from a single point mutation, but also some important differences. Compared to WT, we observe 25% more rupture events for E22G and 15% more mechanically resistant initial conformations (Table 1). In particular, there is an increase by 60% in the number of events with $F_r$ > 150 pN for E22G (40 vs. 25). Our highest $F_r$ is ~260 pN for this variant, compared to ~210 pN for WT (Fig. 2).

The increased number of high-$F_r$ events for the E22G mutant can, at least partly, be traced to a conformational difference noted in our previous work (17,29). Here, we compared the propensities of the four variants WT, E22G, F20E, and E22G/I31E to form turns centered in the 25–30 interval, which is the loop region of the $\beta$-loop-$\beta$ motif in A$\beta$ fibrils (19,20,38). The probability for such turns was found to correlate with the rate of fibril formation, and was, in particular, higher for E22G than for WT (17,29).

If the A$\beta$ molecule is to form a large and potentially force-resistant three-stranded $\beta$-sheet, the 25–30 region is a favorable location for the second turn.

The high-$F_r$ events for E22G can, to a large extent, be linked to three-stranded $\beta$-sheets with $\beta$-structure contents of ~0.7 (Fig. 4). Many of the conformations are in the class with the turns located in the 13–15 and 25–27 regions. In line with the above-mentioned analysis (17,29), we find that the number of rupture events in this conformational class increases from 28 for WT to 53 for E22G. Fig. 6 shows aligned initial conformations and conformations right before rupture for this class, illustrating how the simulations start from a diverse set of conformations that condense to one single structure when pulled.

## $\alpha$S

AFM experiments by different groups have shown that the Parkinson's disease-related $\alpha$S protein can display mechanical resistance (5–7). The set of ~100 pulling trajectories generated and analyzed by Hervás et al. (7) included two in the hyper-mechanostable category ($F_r$ > 400 pN).

Our $\alpha$S study is based on a set of 1024 constant-velocity pulling simulations, two of which are shown in Fig. 1. As in the A$\beta$ study, initial conformations are randomly drawn from a simulated ensemble for the free monomer (18). The $\alpha$S ensemble can be split into two phases: a disordered phase, called D, and a $\beta$-structure-rich phase, B (see Methods for a detailed description). Because the phases are very different, we analyze the two subsets of trajectories separately.

We find that the D phase displays virtually no force resistance. Force peaks >20 pN occur in only 2 of our 449 trajectories started from this phase. In both these runs, the initial energy is close to the cutoff used to distinguish the phases. Among our 575 trajectories started from the B phase, there are, in contrast, only 12 without any force peak >20 pN. The typical B-phase conformation exhibits one large $\beta$-sheet with several strands, often arranged in a simple meander pattern (18). When stretched, it breaks up through a sequence of usually two or three rupture events (Table 1), at each of which a few strands are lost (Fig. 1). Force peaks occurring later in time tend to be higher than
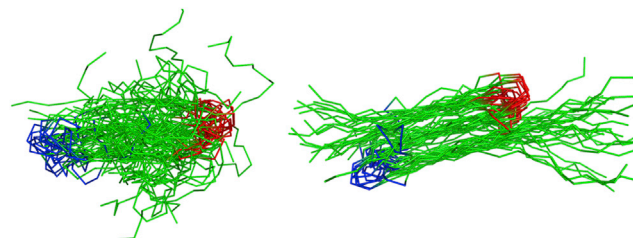


FIGURE 6   Aligned WT A$\beta$ structures before pulling (*left*) and at rupture (*right*) for the 28 observed rupture events in the class with turns at 13–15 and 25–27 (*squares* in Fig. 4). For the initial structures, residues 10–35 were aligned; for the other case, residues 5–35 were aligned.

earlier ones, at least in part because the strands can be more parallel to the applied force as they get fewer in number. In most runs (>90%), the last force peak is associated with the breaking of a three-stranded $\beta$-sheet.

In accord with the observation of conformational polymorphism in AFM experiments (7), our in-total 1464 $\alpha$S rupture events show a wide variation in both $F_r$ and $L_r$ (Fig. 7). The $F_r$ distribution starts to fall off at ~300 pN. The maximum $F_r$ is ~740 pN, but there are only seven events with $F_r > 500$ pN. The $L_r$ distribution exhibits a peak between 35 and 40 nm that can be associated with three-stranded $\beta$-sheets, whereas structures with more strands tend to break at lower $L_r$.

Because $\alpha$S is much larger than A$\beta$, with 140 amino acids instead of 42, a mechanical clamp in $\alpha$S does not have to involve the whole molecule. To locate the parts of $\alpha$S forming clamps in our simulations, we compute a $\beta$-structure profile that represents an average over all rupture events caused by three-stranded $\beta$-sheets (Fig. 5). This profile shows that, although their exact position varies, the force-resistant three-stranded $\beta$-sheets have a statistically preferred sequence location, which is the ~35–65 region. In $\alpha$S fibrils, each molecule is believed to participate in five face-to-face stacked intermolecular $\beta$-sheets (21). Experiments suggest that the five strand regions include the respective stretches 39–41, 52–56, 62–66, 70–77, and 90–94 (21), which are shaded gray in Fig. 5. Our calculated $\beta$-structure profile shows clear similarities with the proposed fibril strand locations. The profile has its three highest peaks in the first three fibril strand regions, and shows signs of shoulders in the remaining two of these regions. As the topology is also the same, a meander pattern, this finding implies that the mechanical clamps observed in our simulations show similarities to the fibril fold. In particular, our results suggest a key mechanical role for the part of $\alpha$S that forms the first three fibril strands.

## DISCUSSION

AFM experiments on the unstructured A$\beta$ and $\alpha$S have observed a very broad range of rupture forces, including
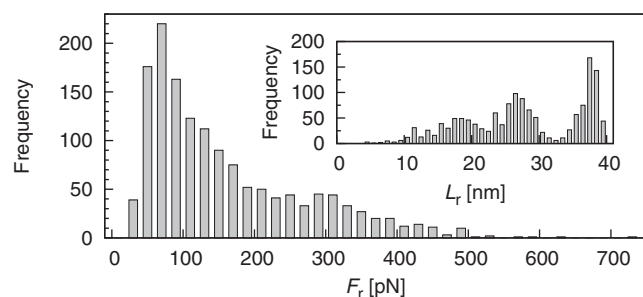


FIGURE 7  Histograms of rupture force, $F_r$, and rupture distance (*inset*), $L_r$, for $\alpha$S, based on a total of 1464 rupture events, 1461 of which are from trajectories started from the B phase.

values of up to 300–400 pN (5–7). The question arises whether these high forces may be due to artifacts such as topological entanglements. One important result of our study is therefore the finding that even the short A$\beta$ peptide can form structures with high mechanical resistance on its own.

There have been previous simulations of other mechanical aspects of proteins implicated in neurodegenerative diseases (39,40). To our knowledge, we are the first, however, to perform calculations that can be directly compared to the AFM pulling experiments on A$\beta$ and $\alpha$S. We can thereby study structural components of the unexpected force resistance found in those experiments.

The force spectra observed in our simulations are comparable to those of the experiments. Furthermore, the vast majority of our high-force rupture events, for both A$\beta$ and $\alpha$S, involve the same type of mechanical clamp, namely a three-stranded $\beta$-sheet with meander topology. The A$\beta$ trajectories only rarely contain more than one force peak. For $\alpha$S, we often observe two or three force peaks, the last and highest of which can be associated with a three-stranded $\beta$-sheet. In hindsight, the form found for the main mechanical clamps appears plausible, especially for A$\beta$. Alternative folds with the same mechanical strength are not easily conceived for a molecule this size.

Mechanical resistance usually stems from $\beta$-sheet structure. On general grounds, one might therefore expect a correlation between the force resistance of a protein and its propensity to form amyloid fibrils (which largely consist of $\beta$-sheets). In line with this picture, and with experiments (7), we find that the aggregation-enhancing E22G mutation increases the mechanical stability of A$\beta$. Its higher force resistance can be linked to an increased occurrence of conformations (Fig. 4) that not only have a high overall $\beta$-structure content, but also display a turn with similarities to the $\beta$-loop-$\beta$ motif in fibrils (19,20,38). Similarly, for $\alpha$S, the most common positions of $\beta$-strands in the strong mechanical clamps (Fig. 5) agree very well with the first three-strand regions in the proposed fibril model (21). The meander-like paths traced out by the A$\beta$ and $\alpha$S backbones in these force-resistant structural units thus show similarities with the proposed fibril folds. These findings hint at a direct structural link between the force resistance of these proteins and their amyloid propensity.

In the A$\beta$ AFM experiments, the fraction of trajectories having at least one force peak >20 pN was 33 and 62% for WT and E22G, respectively (7). In our simulations, the corresponding numbers are 29 ± 1 and 34 ± 4%. A main parameter influencing the amount of force-resistant states is the temperature. Comparison with experimental NMR data suggests that our simulation temperature corresponds to 0–5°C (17). The AFM study was done at room temperature, but the sample was stored at 4°C between experiments. The ensemble probed in the experiments could be influenced by this lower temperature, due to slow

thermalization of Aβ when anchored to a molecular construct. Hence, there are uncertainties about the precise relation between the simulated and experimental ensembles. It is remarkable that the simulated and experimental fractions of trajectories containing rupture events, nevertheless, are within a factor of two of each other for both WT and E22G.

The αS AFM experiments, also performed at room temperature, found 7–45% of the trajectories to contain rupture events (5,7). In our αS simulations, this fraction is <1 and 98% for the D and B phases, respectively. Hence, for a force response matching experimental data, a significant B-phase fraction must be assumed. As previously shown (18), a B-phase fraction of 50–70% is compatible with NMR data at −10°C and −15°C (33,34). However, at room temperature, the free αS monomer is disordered (41), and NMR data at 15°C (32) are well described by the D phase alone (18).

How does one then explain the mechanical resistance seen in room-temperature AFM experiments on αS? Two factors that could affect the AFM ensemble, and push it toward the B phase, are as follows:

First, as discussed for Aβ, due to the kinetically restrictive anchoring to a molecular construct, the AFM ensemble might retain some memory of the low temperature, 4°C, at which the samples were held between experiments.

Second, the anchoring to the molecular construct imposes a constraint on the end-to-end distance, which might disfavor the D phase; the simulated B and D phases have average end-to-end distances of 5.7 nm and 8.1 nm, respectively. We note that Hervás et al. (7), who used a stricter construct, recorded a higher fraction of trajectories containing rupture events, compared to Sandal et al. (5).

The heterogeneous mechanical response revealed by AFM studies (5–7) is not the only indication that β-sheet-containing states are readily accessible to the Aβ and αS monomers. A finding supporting this view is the NMR-derived structure of Aβ in complex with an Affibody protein (42). Beta-sheets formed by the monomers are, of course, different than the intermolecular ones found in fibrils, but transient sampling of such structures might, nevertheless, be important in fibril formation. The addition of a random coil monomer to a growing fibril entails a high cost in conformational entropy, unless the chain is very short. This cost is in part balanced by intermolecular interactions, but a free-energy landscape where intramolecular interactions funnel the monomer toward the fibril fold might be crucial for efficient monomer-fibril association.

Simulation studies of Aβ have been reported by many groups (for recent examples, see the literature (43–50)), which typically observed only very limited amounts of β-structure. We, however, got the best agreement with experimental chemical shifts (30) and J-couplings (31) for an ensemble with a significant fraction of β-sheet-rich states (17). In the pulling simulations presented here, the same β-sheet-rich states can explain the high rupture forces

observed in AFM experiments (Fig. 3). We therefore take the comparisons with AFM data as an independent indication that Aβ need not be as coil-like as commonly thought.

## CONCLUSION

We have examined the structural mechanisms providing the surprisingly high mechanical stability of the unstructured proteins Aβ and αS observed in AFM experiments (5–7), using a large number of pulling simulations with initial conformations randomly drawn from simulated ensembles. Our main findings are as follows:

1. For both Aβ and αS, structures with high force resistance do indeed occur in the simulations, and the main type of mechanical clamp is a β-sheet with three strands of sufficient length, arranged in a meander pattern.
2. The Arctic mutation of Aβ leads to increased occurrence of highly force-resistant structures.
3. The mechanically stable structures of both Aβ and αS show similarities with the respective fibril folds.

These findings suggest that β-sheet-rich force-resistant structures are readily accessible to Aβ and αS and might have a key role in amyloid formation.

## REFERENCES

1. Chiti, F., and C. M. Dobson. 2006. Protein misfolding, functional amyloid, and human disease. *Annu. Rev. Biochem.* 75:333–366.

2. Knowles, T. P. J., and M. J. Buehler. 2011. Nanomechanics of functional and pathological amyloid materials. *Nat. Nanotechnol.* 6:469–479.

3. Eisenberg, D., and M. Jucker. 2012. The amyloid state of proteins in human diseases. *Cell.* 148:1188–1203.

4. Uversky, V. N., and A. K. Dunker. 2010. Understanding protein nonfolding. *Biochim. Biophys. Acta.* 1804:1231–1264.

5. Sandal, M., F. Valle, …, B. Samorì. 2008. Conformational equilibria in monomeric α-synuclein at the single-molecule level. *PLoS Biol.* 6:e6.

6. Brucale, M., M. Sandal, …, B. Samorì. 2009. Pathogenic mutations shift the equilibria of α-synuclein single molecules towards structured conformers. *ChemBioChem.* 10:176–183.

7. Hervás, R., J. Oroz, …, M. Carrión-Vázquez. 2012. Common features at the start of the neurodegeneration cascade. *PLoS Biol.* 10:e1001335.

8. Valbuena, A., J. Oroz, …, M. Carrión-Vázquez. 2009. On the remarkable mechanostability of scaffoldins and the mechanical clamp motif. *Proc. Natl. Acad. Sci. USA.* 106:13791–13796.

9. Sikora, M., J. Sułkowska, …, M. Cieplak. 2011. BSDB: the biomolecule stretching database. *Nucleic Acids Res.* 39:D443–D450.

10. Kirkitadze, M. D., G. Bitan, and D. B. Teplow. 2002. Paradigm shifts in Alzheimer's disease and other neurodegenerative disorders: the emerging role of oligomeric assemblies. *J. Neurosci. Res.* 69:567–577.

11. Bemporad, F., and F. Chiti. 2012. Protein misfolded oligomers: experimental approaches, mechanism of formation, and structure-toxicity relationships. *Chem. Biol.* 19:315–327.

12. Benilova, I., E. Karran, and B. De Strooper. 2012. The toxic A$\beta$ oligomer and Alzheimer's disease: an emperor in need of clothes. *Nat. Neurosci.* 15:349–357.

13. Paci, E., and M. Karplus. 2000. Unfolding proteins by external forces and temperature: the importance of topology and energetics. *Proc. Natl. Acad. Sci. USA.* 97:6521–6526.

14. Klimov, D. K., and D. Thirumalai. 2000. Native topology determines force-induced unfolding pathways in globular proteins. *Proc. Natl. Acad. Sci. USA.* 97:7254–7259.

15. Brockwell, D. J., E. Paci, …, S. E. Radford. 2003. Pulling geometry defines the mechanical resistance of a $\beta$-sheet protein. *Nat. Struct. Biol.* 10:731–737.

16. Carrión-Vázquez, M., H. Li, …, J. M. Fernández. 2003. The mechanical stability of ubiquitin is linkage dependent. *Nat. Struct. Biol.* 10:738–743.

17. Mitternacht, S., I. Staneva, …, A. Irbäck. 2010. Comparing the folding free-energy landscapes of A$\beta$42 variants with different aggregation properties. *Proteins.* 78:2600–2608.

18. Jónsson, S. Æ., S. Mohanty, and A. Irbäck. 2012. Distinct phases of free $\alpha$-synuclein—a Monte Carlo study. *Proteins.* 80:2169–2177.

19. Petkova, A. T., Y. Ishii, …, R. Tycko. 2002. A structural model for Alzheimer's $\beta$-amyloid fibrils based on experimental constraints from solid state NMR. *Proc. Natl. Acad. Sci. USA.* 99:16742–16747.

20. Lührs, T., C. Ritter, …, R. Riek. 2005. 3D structure of Alzheimer's amyloid-$\beta$(1–42) fibrils. *Proc. Natl. Acad. Sci. USA.* 102:17342–17347.

21. Vilar, M., H.-T. Chou, …, R. Riek. 2008. The fold of $\alpha$-synuclein fibrils. *Proc. Natl. Acad. Sci. USA.* 105:8637–8642.

22. Nilsberth, C., A. Westlind-Danielsson, …, L. Lannfelt. 2001. The 'Arctic' APP mutation (E693G) causes Alzheimer's disease by enhanced A$\beta$ protofibril formation. *Nat. Neurosci.* 4:887–893.

23. Irbäck, A., S. Mitternacht, and S. Mohanty. 2009. An effective all-atom potential for proteins. *PMC Biophys.* 2:2.

24. Mitternacht, S., S. Luccioli, …, A. Irbäck. 2009. Changing the mechanical unfolding pathway of FnIII$_{10}$ by tuning the pulling strength. *Biophys. J.* 96:429–441.

25. Evans, E., and K. Ritchie. 1997. Dynamic strength of molecular adhesion bonds. *Biophys. J.* 72:1541–1555.

26. Tiana, G., L. Sutto, and R. A. Broglia. 2007. Use of the Metropolis algorithm to simulate the dynamics of protein chains. *Physica A.* 380:241–249.

27. Vitalis, A., and R. V. Pappu. 2009. Methods for Monte Carlo simulations of biomacromolecules. *Annu. Rep. Comput. Chem.* 5:49–76.

28. Favrin, G., A. Irbäck, and F. Sjunnesson. 2001. Monte Carlo update for chain molecules: biased Gaussian steps in torsional space. *J. Chem. Phys.* 114:8154–8158.

29. Mitternacht, S., I. Staneva, …, A. Irbäck. 2011. Monte Carlo study of the formation and conformational properties of dimers of A$\beta$42 variants. *J. Mol. Biol.* 410:357–367.

30. Hou, L., H. Shao, …, M. G. Zagorski. 2004. Solution NMR studies of the A$\beta$(1–40) and A$\beta$(1–42) peptides establish that the Met$^{35}$ oxidation state affects the mechanism of amyloid formation. *J. Am. Chem. Soc.* 126:1992–2005.

31. Sgourakis, N. G., Y. Yan, …, A. E. García. 2007. The Alzheimer's peptides A$\beta$40 and 42 adopt distinct conformations in water: a combined MD/NMR study. *J. Mol. Biol.* 368:1448–1457.

32. Eliezer, D., E. Kutluay, …, G. Browne. 2001. Conformational properties of $\alpha$-synuclein in its free and lipid-associated states. *J. Mol. Biol.* 307:1061–1073.

33. Kim, H.-Y., H. Heise, …, M. Zweckstetter. 2007. Correlation of amyloid fibril $\beta$-structure with the unfolded state of $\alpha$-synuclein. *ChemBioChem.* 8:1671–1674.

34. Wu, K.-P., S. Kim, …, J. Baum. 2008. Characterization of conformational and dynamic properties of natively unfolded human and mouse $\alpha$-synuclein ensembles by NMR: implication for aggregation. *J. Mol. Biol.* 378:1104–1115.

35. Frishman, D., and P. Argos. 1995. Knowledge-based protein secondary structure assignment. *Proteins.* 23:566–579.

36. Hubbard, S. J., and J. M. Thornton. 1993. NACCESS Computer Program. Department of Biochemistry and Molecular Biology, University College London, London, UK.

37. DeLano, W. L. 2002. The PyMOL Molecular Graphics System. DeLano Scientific, San Carlos, CA.

38. Ahmed, M., J. Davis, …, S. O. Smith. 2010. Structural conversion of neurotoxic amyloid-$\beta_{1-42}$ oligomers to fibrils. *Nat. Struct. Mol. Biol.* 17:561–567.

39. Raman, E. P., T. Takeda, …, D. K. Klimov. 2007. Mechanical unbinding of A$\beta$ peptides from amyloid fibrils. *J. Mol. Biol.* 373:785–800.

40. Das, A., and S. S. Plotkin. 2013. SOD1 exhibits allosteric frustration to facilitate metal binding affinity. *Proc. Natl. Acad. Sci. USA.* 110:3871–3876.

41. Weinreb, P. H., W. Zhen, …, P. T. Lansbury. 1996. NACP, a protein implicated in Alzheimer's disease and learning, is natively unfolded. *Biochemistry.* 35:13709–13715.

42. Hoyer, W., C. Grönwall, …, T. Härd. 2008. Stabilization of a $\beta$-hairpin in monomeric Alzheimer's amyloid-$\beta$ peptide inhibits amyloid formation. *Proc. Natl. Acad. Sci. USA.* 105:5099–5104.

43. Wu, C., J. Scott, and J.-E. Shea. 2012. Binding of Congo Red to amyloid protofibrils of the Alzheimer A$\beta_{1-40}$ peptide probed by molecular dynamics simulations. *Biophys. J.* 103:550–557.

44. Lockhart, C., S. Kim, and D. K. Klimov. 2012. Explicit solvent molecular dynamics simulations of A$\beta$ peptide interacting with ibuprofen ligands. *J. Phys. Chem. B.* 116:12922–12932.

45. Lemkul, J. A., and D. R. Bevan. 2012. Morin inhibits the early stages of amyloid $\beta$-peptide aggregation by altering tertiary and quaternary interactions to produce "off-pathway" structures. *Biochemistry.* 51:5990–6009.

46. Côté, S., R. Laghaei, …, N. Mousseau. 2012. Distinct dimerization for various alloforms of the amyloid-$\beta$ protein: A$\beta_{1-40}$, A$\beta_{1-42}$, and A$\beta_{1-40}$(D23N). *J. Phys. Chem. B.* 116:4043–4055.

47. Viet, M. H., and M. S. Li. 2012. Amyloid peptide A$\beta$40 inhibits aggregation of A$\beta$42: evidence from molecular dynamics simulations. *J. Chem. Phys.* 136:245105.

48. Chong, S.-H., and S. Ham. 2012. Impact of chemical heterogeneity on protein self-assembly in water. *Proc. Natl. Acad. Sci. USA.* 109:7636–7641.

49. Barz, B., and B. Urbanc. 2011. Dimer formation enhances structural differences between amyloid $\beta$-protein (1–40) and (1–42): an explicit-solvent molecular dynamics study. *PLoS ONE.* 7:e34345.

50. Velez-Vega, C., and F. A. Escobedo. 2011. Characterizing the structural behavior of selected A$\beta$-42 monomers with different solubilities. *J. Phys. Chem. B.* 115:4900–4910.